JACS
JOURNAL OF THE AMERICAN CHEMICAL SOCIETY
Article
pubs.acs.org/JACS

Monitoring the Reaction Process During the $S_2 \rightarrow S_3$ Transition in Photosynthetic Water Oxidation Using Time-Resolved Infrared Spectroscopy

Hiroki Sakamoto, Tatsuki Shimizu, Ryo Nagao, and Takumi Noguchi*

Division of Material Science, Graduate School of Science, Nagoya University, Furo-cho, Chikusa-ku, Nagoya 464-8602, Japan

Supporting Information

ABSTRACT: Photosynthetic water oxidation performed at the Mn_4CaO_5 cluster in photosystem II plays a crucial role in energy production as electron and proton sources necessary for CO_2 fixation. Molecular oxygen, a byproduct, is a source of the oxygenic atmosphere that sustains life on earth. However, the molecular mechanism of water oxidation is not yet well-understood. In the reaction cycle of intermediates called S states, the $S_2 \rightarrow S_3$ transition is particularly important; it consists of multiple processes of electron transfer, proton release, and water insertion, and generates an intermediate leading to O−O bond formation. In this study, we monitored the reaction process during the $S_2 \rightarrow S_3$ transition using time-resolved infrared spectroscopy to clarify its molecular mechanism. A change in the hydrogen-bond interaction of the oxidized $Y_Z^\bullet$ radical, an immediate electron acceptor of the Mn_4CaO_5 cluster, was clearly observed as a ∼100 μs phase before the electron-transfer phase with a time constant of ∼350 μs. This observation provides strong experimental evidence that rearrangement of the hydrogen-bond network around $Y_Z^\bullet$, possibly due to the movement of a water molecule located near $Y_Z^\bullet$ to the Mn site, takes place before the electron transfer. The electron transfer was coupled with proton release, as revealed by a relatively high deuterium kinetic isotope effect of 1.9. This proton release, which decreases the redox potential of the Mn_4CaO_5 cluster to facilitate electron transfer to $Y_Z^\bullet$, was proposed to determine, as a rate-limiting step, the relatively slow electron-transfer rate of the $S_2 \rightarrow S_3$ transition.

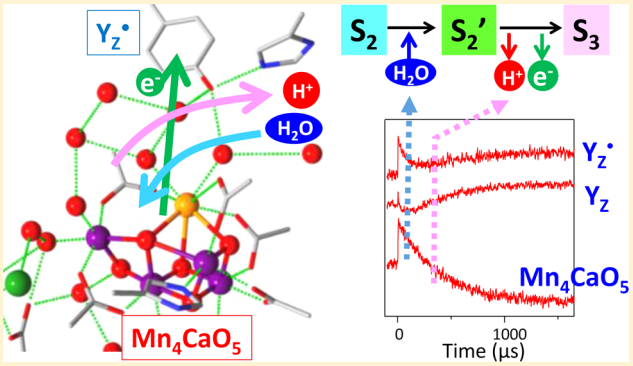

INTRODUCTION

Photosynthetic water oxidation performed by plants and cyanobacteria is one of the most essential biological processes in bioenergy production. It produces electrons, protons, and molecular oxygen using solar energy. The electrons are used to produce NADPH as a reducing power, while the protons contribute to the formation of a proton gradient across thylakoid membranes to produce ATP. The NADPH and ATP are then used to synthesize sugars from CO_2. In contrast, molecular oxygen is a waste product; however, it is a major source of oxygen in the atmosphere necessary for respiration. In addition, oxygen forms an ozone layer, which protects life from harmful UV light. Thus, photosynthetic water oxidation sustains life on earth as energy and oxygen sources.

The water oxidation reaction is performed in photosystem II (PSII) protein complexes embedded in thylakoid membranes.[1−6] In PSII, light-induced charge separation takes place between the primary donor chlorophyll (P680) and the pheophytin electron acceptor (Pheo) to generate a charged pair, $P680^+Pheo^-$. The electron on $Pheo^-$ is transferred to the quinone electron acceptors, Q_A and Q_B, while the electron hole on $P680^+$ is transferred to the redox tyrosine Y_Z, which then becomes a $Y_Z^\bullet$ radical by shifting a proton to a neighboring His residue (D1-H190) through a strong hydrogen bond. The $Y_Z^\bullet$ further oxidizes the Mn_4CaO_5 cluster (Figure 1A),[7,8] which is the inorganic core of the water oxidizing center (WOC), the catalytic site of water oxidation. In the WOC, two water molecules are oxidized to one molecular oxygen and four protons though the cycle of five intermediates called S_i states (i = 0−5) (Figure 1B),[9,10] where a larger i value represents a higher oxidation state of the Mn_4CaO_5 cluster. Among these S states, the S_1 state is the most stable in the dark. Short-flash illumination advances an S_i state to the next S_{i+1} state by electron abstraction by the $Y_Z^\bullet$ radical (Figure 1B). The highest-oxidized S_4 state is a transient state and immediately relaxes to the S_0 state by releasing a molecular oxygen. The proton release pattern has been estimated as 1:0:1:2 for the $S_0 \rightarrow S_1$, $S_1 \rightarrow S_2$, $S_2 \rightarrow S_3$, and $S_3 \rightarrow S_0$ transitions,[11,12] and hence an excessive positive charge resides on the Mn_4CaO_5 cluster at the S_2, S_3, and S_4 states.

In the S-state cycle, the $S_2 \rightarrow S_3$ transition is a particularly important process; the formed S_3 state is a metastable intermediate that leads to the O−O bond formation in the next transition, and hence its structure should provide crucial information for understanding the chemical mechanism of O_2

Received: November 21, 2016
Published: January 16, 2017

DOI: 10.1021/jacs.6b11989
J. Am. Chem. Soc. 2017, 139, 2022−2029

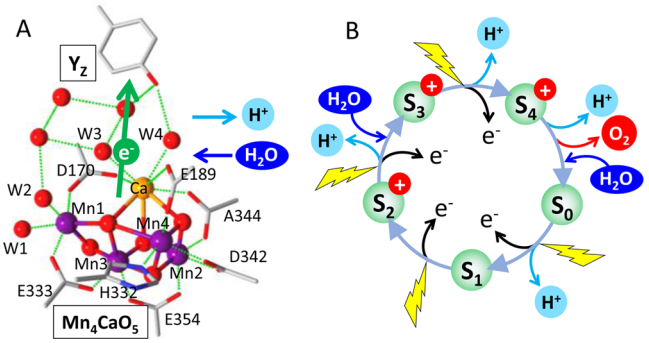

Figure 1. (A) Structure of the Mn_4CaO_5 cluster and the interaction with Y_Z. (B) S-state cycle of water oxidation. The amino acid ligands of the Mn_4CaO_5 cluster are on the D1 subunit except for E354, which is on the CP43 subunit. Atomic coordinates from the X-ray crystallographic structure (PDB code: 4UB6)[8] were used to generate the image in panel A.

formation. In contrast to the $S_1 \rightarrow S_2$ transition, which is rather a simple process of oxidation of the Mn_4CaO_5 cluster, the $S_2 \rightarrow S_3$ transition involves a proton release reaction coupled with electron transfer.[3,5] Because of the presence of an excessive positive charge in the S_2 state, proton release was proposed to take place before electron transfer to remove a positive charge from the catalytic site and reduce the redox potential of the Mn_4CaO_5 cluster.[13−16] In addition, the results of Fourier transform infrared (FTIR) studies[17−19] and recent theoretical studies[20−27] have suggested that a water molecule is inserted into the WOC in the $S_2 \rightarrow S_3$ transition. Theoretical studies have also predicted that the water insertion to the Mn site is coupled with the interconversion of the "open" and "closed" cubane conformations of the S_2 state. In these proton release and water insertion processes of the $S_2 \rightarrow S_3$ transition, the hydrogen-bond network of water molecules near Ca (Figure 1A) may play an important role,[24,25,28] because Ca^{2+} depletion blocks the $S_2 \rightarrow S_3$ transition.[1,29] Thus, the $S_2 \rightarrow S_3$ transition is a rather complex process that involves electron, proton, and water transfers, and clarifying the details of this process involving the structural changes of the water network is crucial for a full understanding of the whole mechanism of water oxidation.

The kinetics of the $S_2 \rightarrow S_3$ transition have been investigated by time-resolved measurements of various spectroscopic techniques, such as UV absorption,[30−33] electron spin resonance (EPR),[34,35] X-ray absorption,[36,37] and infrared absorption.[15] These studies have indicated that the $S_2 \rightarrow S_3$ transition takes place in a major phase with a time constant of 200−500 μs, which has been assigned to the electron transfer from the Mn_4CaO_5 cluster to $Y_Z^{\bullet}$. In addition, the temperature dependence of the kinetics of UV absorption showed that the $S_2 \rightarrow S_3$ transition has the highest activation energy among the four S-state transitions,[4,32] suggesting that this phase is not a simple electron-transfer reaction. Recently, Dau and co-workers[13,14] found a 30 μs phase with a large kinetic isotope effect (KIE) of 4−5 in the $S_2 \rightarrow S_3$ transition based on photothermal beam deflection (PBD) measurements, and assigned it to the proton release process that takes place before electron transfer. A very recent X-ray absorption study by the same group also supported this result.[37] In contrast, a 30−50 μs phase has been observed in the $P680^+$ decay in time-resolved absorption and fluorescence measurements,[38−40] and this phase has been attributed to the last step of hole transfer from $P680^+$ to Y_Z reflecting the relaxation of the protein environment around Y_Z.[4]

In this study, we investigated the details of the reaction process of the $S_2 \rightarrow S_3$ transition using time-resolved infrared (TRIR) spectroscopy. With this spectroscopy, we can monitor the time courses of the structural changes and reactions of individual cofactors or specific sites in proteins by time-dependent detection of the changes in infrared absorption by characteristic vibrations of the target sites. In our previous TRIR study of the S-state transitions,[15,16] we monitored the time courses at 1400 and 2500 cm^{-1}, with the wavenumbers representing the vibrations of carboxylate groups[41−43] and strongly hydrogen-bonded water molecules,[28,44] respectively, around the Mn_4CaO_5 cluster. In the $S_2 \rightarrow S_3$ transition, in addition to a major electron-transfer phase with a 300−500 μs time constant, an earlier phase of ~70 μs was observed in the 2500 cm^{-1} trace. Although this phase was temporarily assigned to the proton release before electron transfer,[15] a definite conclusion could not be reached without further detailed analyses. In this work, we applied improved measurement conditions compared with the previous study:[15] 10-times higher time resolution (~2.5 μs) to resolve an early phase, measurements in both H_2O and D_2O to estimate KIE, and monitoring the reactions of Y_Z, $Y_Z^{\bullet}$, and $P680^+$ in addition to the Mn_4CaO_5 cluster and the water network. We observed a clear phase representing the rearrangement of the hydrogen-bond network around $Y_Z^{\bullet}$, possibly due to water movement, before the electron-transfer phase. It was further found that the electron transfer was coupled with a proton release process functioning as a rate-limiting step. With the obtained results in combination with previous theoretical predictions, we propose a model of the molecular mechanism of the $S_2 \rightarrow S_3$ transition.

MATERIALS AND METHODS

Preparation of Samples. Oxygen-evolving PSII core complexes of *Thermosynechococcus elongatus*, in which the C-terminus of the CP47 subunit was histidine tagged,[45] were isolated following the method described previously.[46] An aliquot of the sample suspension (~10 mg Chl/mL; 10 μL) in a 1 mM 2-(*N*-morpholino)ethanesulfonic acid (MES) buffer (pH 6.0) containing 5 mM NaCl, 5 mM $CaCl_2$, and 0.03% n-dodecyl β-D-maltoside mixed with 1 μL of 100 mM potassium ferricyanide solution was deposited on a CaF_2 plate (25 mm in diameter), and lightly dried under N_2 gas flow. The sample was then mixed with 1 μL of a 200 mM MES buffer (pH 6.0), and this solution was sandwiched with another CaF_2 plate with a circular groove (10 mm inner diameter; 1 mm width).[12] The sample cell was sealed with silicone grease in the outer part of the groove, where a tiny piece of aluminum foil was placed as a spacer. For D_2O exchange, the above sample suspended in a 200 mM MES buffer was lightly dried and then resuspended in 5 μL of D_2O (Cambridge Isotope Laboratories, Inc., 99.9 atom % D). After repeating this procedure of drying and suspending in D_2O twice, the dried sample was mixed with 1 μL of D_2O and then sandwiched with another CaF_2 plate in the same way as the H_2O sample. The sample temperature was maintained at 10 °C by circulating cold water in a copper holder.

TRIR Measurements. The TRIR measurements were performed following the method described previously.[15] Monitoring IR light, from which visible light was removed by a Ge filter (>4200 cm^{-1} cut), was dispersed using an IR grating monochromator (JASCO, TRIR-1000) after passing through the sample and focused onto an MCT detector (Infrared, MCT-10-1.0) coupled with a preamplifier (Infrared, MCT-1000). The signal was amplified using a second amplifier (Stanford Research Systems, model SR560) and recorded on a 1 GHz digital oscilloscope (LeCroy, WaveRunner 610Zi). The bandwidth of the second amplifier was 100 kHz to 1 Hz, which provides a time resolution of ~2.5 μs (Figure S1). The sample was excited by a Q-

DOI: 10.1021/jacs.6b11989
J. Am. Chem. Soc. 2017, 139, 2022−2029

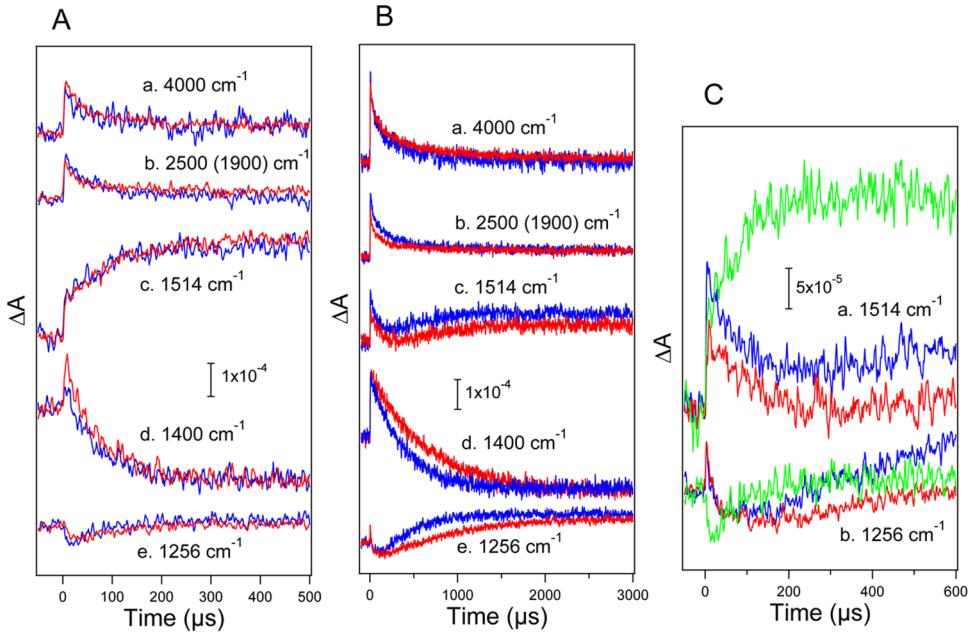

Figure 2. Time course of ΔA at 4000 (a), 2500 (1900 in D_2O) (b), 1514 (c), 1400 (d), and 1256 (e) cm^{-1} during the $S_1 \rightarrow S_2$ (A) and $S_2 \rightarrow S_3$ (B) transitions. PSII core complexes were suspended in H_2O (blue lines) or D_2O (red lines) buffers (pL 6.0). The sample temperature was 10 °C. (C) Time course in an early time region (0−600 μs) at 1514 (a) and 1256 (b) cm^{-1} during the $S_2 \rightarrow S_3$ transition (blue lines, in H_2O; red lines, in D_2O) compared with that during the $S_1 \rightarrow S_2$ transition (green lines, in H_2O).

switched Nd:YAG laser (INDI-40-10; 532 nm; ~7 ns fwhm). The scheme of laser flash illumination and data acquisition is shown in Figure S2. Two preflashes (2 s interval) with a saturating power (~7 mJ $pulse^{-1}$ cm^{-2}) were first applied to the sample followed by dark relaxation for 40 min (50 min for D_2O sample) so that the WOC was synchronized to the S_1 state. Two flashes (~7 mJ $pulse^{-1}$ cm^{-2}; 2 s interval) were then applied, and an IR absorption change upon each flash was recorded from −300 μs to 10 ms with 1 μs/point. After dark relaxation for 40 min (50 min in D_2O), a four times stronger flash (~28 mJ $pulse^{-1}$ cm^{-2}) was applied, and the absorption change was recorded. This measurement using a stronger flash was necessary to obtain a heat-induced signal (see SI for details about a heat signal). These measurements at two flashes and a subsequent stronger flash were repeated at a 40 min (50 min in D_2O) interval. The period of the dark interval was determined by the relaxation time of the S_3 state to the S_1 state, which was estimated by detecting a signal intensity at the second flash while changing the interval from a longer to a shorter period. The spectral resolution of the monochromator was 32, 24, 16, 16, and 16 cm^{-1} at 4000, 2500 (1900 in D_2O), 1514, 1400, and 1256 cm^{-1}, respectively. The results of 4, 10, 27, 48, and 48 measurements in H_2O and 2, 2, 56, 16, 38 measurements in D_2O were averaged for final data at 4000, 2500 (1900 in D_2O), 1514, 1400, and 1256 cm^{-1}, respectively. Data analysis by global fitting of the time courses involving convolution with an instrumental function was performed using IGOR Pro (Wavemetrics Inc.).

RESULTS

We selected seven different wavenumbers of probing IR light to monitor the time-dependent behaviors of different cofactors and water molecules involved in the $S_2 \rightarrow S_3$ transition. $P680^+$ has a broad intervalence band centered at 4000 cm^{-1} (Figure S3A, inset);[47] hence, 4000 cm^{-1} was used to monitor the behavior of $P680^+$ in the microsecond time region. Strong hydrogen bonds in a hydrogen-bond network involving water molecules near the Mn_4CaO_5 cluster show a broad feature in 3000−2400 cm^{-1} (Figure S3Ac,d).[28,44] Thus, 2500 cm^{-1} was used to detect the changes in the hydrogen-bond network around the Mn_4CaO_5 cluster. The NH stretching vibration of D1-His190 forming a strong hydrogen bond with $Y_Z^\bullet$ (Figure S3Ab)[46] and a broad positive feature of $P680^+$ (Figure S3Aa)[47] also contribute to this wavenumber. These strongly hydrogen-bonded OH and NH vibrations largely downshift to the 2400−1800 cm^{-1} region in D_2O as deuterium-bonded OD and ND vibrations (Figure S3A, red lines),[28,46] and hence 1900 cm^{-1} was used to monitor the change in the deuterium-bond network for a sample in D_2O. The electron transfer and the interaction change of the Mn_4CaO_5 cluster was monitored at 1400 cm^{-1}, where strong COO^- bands with negative intensities appear in both the S_2/S_1 and S_3/S_2 FTIR difference spectra (Figure S3Bc,d).[16,41−43,48] Note that the two conformations (open and closed cubane structures) of the S_2 state provide rather similar infrared features in the COO^- region,[43,49] and hence, they are difficult to discriminate clearly. $Y_Z^\bullet$ and Y_Z have CO stretching bands at 1514 and 1256 cm^{-1}, respectively (Figure S3Bb),[46,50,51] and hence, these wavenumbers were used to monitor the behaviors and hydrogen-bond changes of $Y_Z^\bullet$ and Y_Z. It should be noted that these bands of $Y_Z^\bullet$ and Y_Z are not strongly affected by H/D exchange (Figure S3Bb, red line). The S_2/S_1 and S_3/S_2 difference spectra also showed positive signals at these frequencies due to the asymmetric COO^- and amide II vibrations (Figure S3Bc,d).[42]

The IR absorption changes at these wavenumbers upon the first-flash illumination provided the time courses of the reactions and the structural changes of individual cofactors and their surroundings during the $S_1 \rightarrow S_2$ transition (Figure 2A). Note that these traces were obtained after correction of a heat effect induced by laser illumination (see Supporting Information for details of heat-effect correction). All the traces at different wavenumbers showed relatively simple decay curves. Because these traces should reflect the same reaction process, global fitting of all the traces with common time constants is the best method of analysis. Global fit analysis using a double exponential function convoluted by an instrumental function (Figure S1, blue line) provided time

DOI: 10.1021/jacs.6b11989
J. Am. Chem. Soc. 2017, 139, 2022−2029

constants of 12 ± 2 and 72 ± 2 μs in H_2O (Table 1; fitting curves and exponential components are shown in Figure 3). In

Table 1. Time Constants of the $S_1 \rightarrow S_2$ and $S_2 \rightarrow S_3$ Transitions and Kinetic Isotope Effects (KIE) Estimated by Global Fit Analysis of the Time Courses of IR Absorption Changes

	$S_1 \rightarrow S_2$		$S_2 \rightarrow S_3$		
	τ_1 (μs)	τ_2 (μs)	τ_1 (μs)	τ_2 (μs)	τ_3 (μs)
H_2O[a]	12 ± 2	72 ± 2	13 ± 1	104 ± 4	352 ± 3
D_2O[a]	16 ± 1	85 ± 2	14 ± 1	122 ± 3	663 ± 4
KIE	1.4 ± 0.4	1.2 ± 0.1	1.1 ± 0.2	1.2 ± 0.1	1.9 ± 0.1

[a]Errors are standard deviations of the time constants as fitting parameters in global fit analysis.

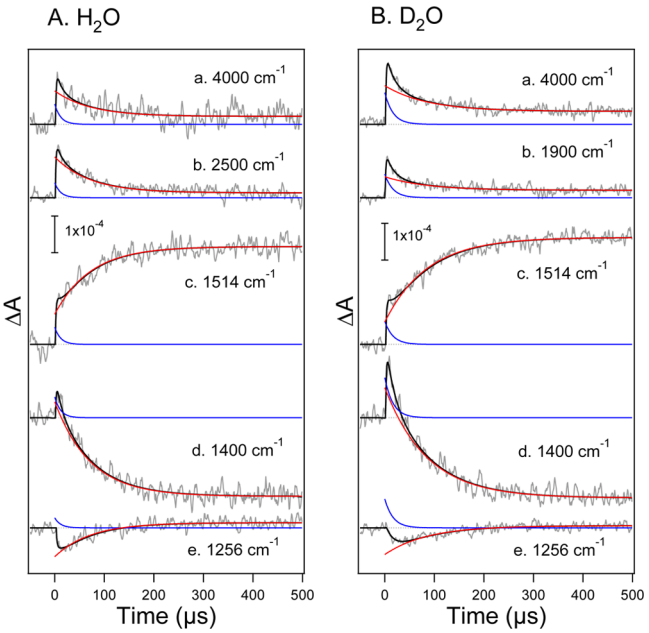

Figure 3. Results of the global fit analysis of the TRIR traces of the $S_1 \rightarrow S_2$ transition measured in H_2O (A) and D_2O (B). Fitting curves (black lines) on the experimental data (gray lines) were obtained by convolution of a double exponential function (blue and red lines for faster and slower components, respectively) with the instrumental function (Figure S1, blue line).

D_2O, slightly slower time constants of 16 ± 1 and 85 ± 2 μs were obtained (Figure 3), providing KIE values of 1.4 ± 0.4 and 1.2 ± 0.1, respectively. Thus, a relatively small effect of H/D exchange was observed in the $S_1 \rightarrow S_2$ transition, which is consistent with the fact that this transition is not accompanied by proton release from WOC[11,12] and only involves a proton shift from D1-His190 to $Y_Z^\bullet$ when $Y_Z^\bullet$ is re-reduced. The ~70 μs time constant of the major phase is consistent with the previous reports.[15,30−36]

The time courses at individual frequencies in the $S_2 \rightarrow S_3$ transition are presented in Figure 2B. These traces were measured upon the second flash followed by corrections for heat effect (Figure S5) and miss probability. The miss probability was estimated to be 10 ± 2% by simulation of the flash-number dependence of the intensity at 6 ms in the traces at 1400 cm^{-1} obtained by 12 consecutive flashes (Figure S7). This miss probability is virtually identical to that in our previous FTIR measurements for the solution sample of *Thermosynechococcus elongatus* PSII core complexes.[12,52,53] The retarded decays in D_2O were clearly seen in the time courses of the COO^- ligands of the Mn_4CaO_5 cluster (1400 cm^{-1}) and the CO vibration of Y_Z (1256 cm^{-1}) (Figure 2Bd,e, red lines). In addition, characteristic behaviors were observed in early phases of $Y_Z^\bullet$ (1514 cm^{-1}) and Y_Z (1256 cm^{-1}). The intensity at 1514 cm^{-1} decreased at about 100 μs and then increased to reach a positive intensity arising from the S_3 state of the Mn_4CaO_5 cluster (the expanded figure is shown in Figure 2Ca). During this period, there is a lag before the rise of intensity in the trace of the reduced Y_Z at 1256 cm^{-1} (Figure 2Be,Cb, blue and red lines). Note that these characteristics of the time courses were not affected by changing the assumption of the miss probability between 5% and 15% (Figure S8). In addition, the trend of the time courses in the $S_2 \rightarrow S_3$ transition is considerably different from that in the $S_1 \rightarrow S_2$ transition at these wavenumbers, which showed a rise of intensities during this period (Figure 2C, green lines). Therefore, these behaviors are not attributed to the contamination with the $S_1 \rightarrow S_2$ transition. In addition, the possibility of the contribution of artifacts such as the heat effect can be excluded, because if such artifacts were present, they would be involved also in the traces of the $S_1 \rightarrow S_2$ transition.

Because it is now clear that there is an early phase at about 100 μs before the main phase, which has a slower but close time constant, the reaction kinetics should be analyzed by a consecutive reaction consisting of three components with two time constants. In addition, there is a faster phase clearly seen at 4000, 2500, and 1256 cm^{-1} (Figure 2C). This phase seems rather separated from the next phase at ~100 μs, and hence, it may be treated as an additional exponential decay. Thus, the $S_2 \rightarrow S_3$ traces were analyzed with eq 1, which consists of a single exponential for a fast-decay component (designated as A) and a consecutive reaction (B → C → D), convoluted with an instrumental function (Figure S1, blue line).

$$f(t) = I_A e^{-t/\tau_1} + I_B e^{-t/\tau_2} + I_C \frac{\tau_2^{-1}}{\tau_3^{-1} - \tau_2^{-1}}(e^{-t/\tau_2} - e^{-t/\tau_3}) + I_D\left(1 - \frac{\tau_3^{-1}}{\tau_3^{-1} - \tau_2^{-1}} e^{-t/\tau_2} + \frac{\tau_2^{-1}}{\tau_3^{-1} - \tau_2^{-1}} e^{-t/\tau_3}\right) \quad (1)$$

Here, the following abbreviations apply: τ_1 is the time constant of the fast exponential decay, τ_2 and τ_3 are the time constants of the first and second phases, respectively, of the consecutive reaction, and I_A, I_B, I_C, and I_D are the IR intensities of the component A, B, C, and D, respectively. Again, global fit analysis with common time constants should be the best way to analyze the traces reflecting the same reaction process. All the trances were well-fitted by this equation with three time constants in Table 1 (Figure 4). The fastest decay phase has a time constant of 13 ± 1 μs with a small KIE of 1.1 ± 0.2. The time constant of the first phase of a consecutive reaction is 104 ± 4 μs. This phase showed a relatively small KIE of 1.2 ± 0.1, which is typically seen in the absence of a large D_2O-induced change in the ~100 μs phase in the trace of $Y_Z^\bullet$ at 1514 cm^{-1} (Figure 2Ca, blue and red lines). The slowest phase showed a time constant of 352 ± 3 μs, which substantially increased to 663 ± 4 μs in D_2O and thus showed a relatively large KIE of 1.9 ± 0.1. The contributions of individual components to each fitting curve obtained by the global fit are shown in Figure 4

DOI: 10.1021/jacs.6b11989
J. Am. Chem. Soc. 2017, 139, 2022−2029

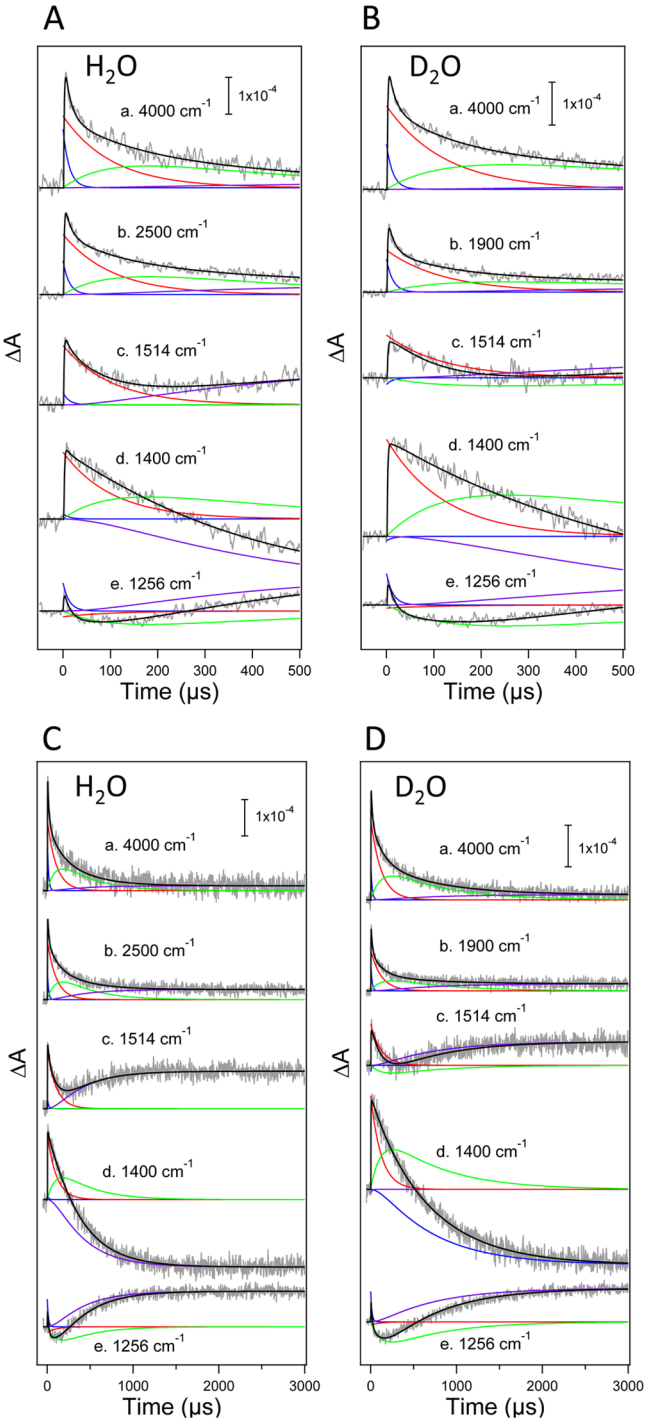

Figure 4. Results of global fit analysis of the TRIR traces of the $S_2 \rightarrow S_3$ transition measured in H_2O (A, 0–500 μs; C, 0–3000 μs) and D_2O (B, 0–500 μs; D, 0–3000 μs). Experimental curves (gray lines) are overlaid with fitting curves (black lines), which were obtained by convolution of the sum of four components (blue, red, green, and purple lines for components A, B, C, and D, respectively) with the instrumental function. See text for details.

(the amplitudes of individual components are presented in Table S1).

To further examine the origin of the early phase in the trace of $Y_Z^{\bullet}$, we scanned wavenumbers around 1514 cm^{-1} (1534–1494 cm^{-1}) to monitor the time courses of absorption changes (Figure 5A). Global fit analysis using eq 1 and the time

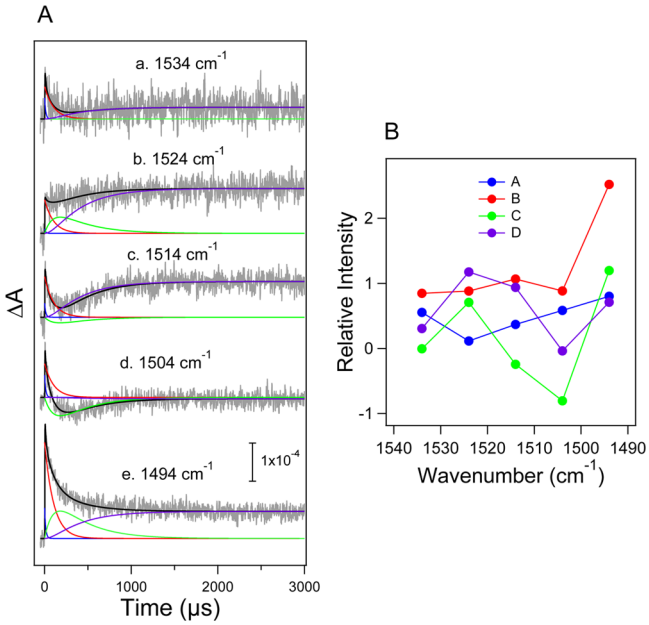

Figure 5. Time course of ΔA in the CO stretching region of $Y_Z^{\bullet}$ (1534–1494 cm^{-1}) measured in H_2O overlaid with the result of global fit analysis (A), and the spectra of individual components (B). See the caption of Figure 4 for the meaning of the colored lines in panel A.

constants obtained by the above analysis (i.e., 13, 104, and 352 μs) provided the spectra of individual components (Figure 5B). The 104 μs phase corresponds to the decay and rise of the first (B) and second (C) components, respectively, of the consecutive reaction. The peak at 1514 cm^{-1} in component B (red circles) is upshifted to 1524 cm^{-1} in component C (green circles). Thus, the 104 μs phase represents the upshift of the CO band of $Y_Z^{\bullet}$ by ~10 cm^{-1}, indicative of the interaction change at the CO group. Because previous studies have shown that stronger hydrogen bonding upshifts the CO frequency of a tyrosine neutral radial,[50,51] the observed upshift of the $Y_Z^{\bullet}$ CO frequency (Figure 5B) suggests that the hydrogen-bond interaction is strengthened during this phase.

DISCUSSION

The TRIR measurements conducted in this study monitored the reactions or interaction changes of the Mn_4CaO_5 cluster; the nearby water network; and Y_Z, $Y_Z^{\bullet}$, and $P680^+$ during the $S_2 \rightarrow S_3$ transition in the microsecond time range (Figure 2B). Global fit analysis showed that all the traces were well-fitted with three phases with time constants of 13 ± 1, 104 ± 4, and 352 ± 3 μs (Figure 4 and Table 1). The faster two phases showed relatively small KIE values of 1.1 and 1.2, respectively, whereas the slowest phase showed a larger KIE of 1.9.

The major ~350 μs phase mainly contributes to the time courses of IR absorption changes at 1514, 1256, and 1400 cm^{-1} due to $Y_Z^{\bullet}$, Y_Z, and Mn_4CaO_5 cluster, respectively (Figure 4). This time constant is in good agreement with that in the previous time-resolved studies using various spectroscopies,[15,30−36] in which the phase of 200–500 μs was assigned to the electron transfer from the Mn_4CaO_5 cluster to $Y_Z^{\bullet}$. The KIE of ~2 of this phase (Table 1) also agrees with the previous data.[14,32] The fastest ~10 μs phase, which has a relatively large contribution to the trace at 4000 cm^{-1} arising from the intervalence transition of $P680^+$ (Figure 4; Table S1), could originate from the microsecond component of $P680^+ \rightarrow Y_Z$

DOI: 10.1021/jacs.6b11989
J. Am. Chem. Soc. 2017, 139, 2022–2029

hole transfer in a minor population involving a protein conformational change around Y_Z, which has been proposed by Renger as the origin of the ~35 μs component of the $P680^+$ decay.[4] The possibility that WOC-inactivated centers partially involved in the sample contribute to this slow $P680^+$ decay cannot be excluded at the present stage.

The ~100 μs phase was clearly observed as changes in the hydrogen-bond interaction of the $Y_Z^\bullet$ CO (1514 cm^{-1}) and a lag phase before the Y_Z recovery (1256 cm^{-1}) (Figure 2C). It also showed large contributions to the changes in the water network (2500 cm^{-1}) and the COO^- groups around the Mn_4CaO_5 cluster (1400 cm^{-1}) (Figure 4 and Table S1), although such contributions were not clear without a fitting procedure because of the monotonic decay curves. The ~70 μs decay in the trace at 2500 cm^{-1} observed in our previous TRIR study[15] corresponds to this ~100 μs phase. Although we previously assigned this phase to proton release before electron transfer, the current study showed that the time constant of this phase is not especially sensitive to H/D exchange and provides a relatively small KIE of 1.2. This value is smaller than a typical KIE value of 1.4−1.5 for the proton mobility in solution accompanied by water reorientation.[54,55] Thus, this phase may not originate from proton release to the bulk through a proton channel in the protein, but rather from the rearrangement of a hydrogen-bond network due to water reorientation, possibly coupled with internal proton transfer. Indeed, the CO frequency of $Y_Z^\bullet$ upshifted by ~10 cm^{-1} in this phase (Figure 5B), indicating the change in the hydrogen-bond interaction of the $Y_Z^\bullet$ CO probably by rearrangement of the water molecules interacting with $Y_Z^\bullet$. In addition, the relatively large contributions of this phase to the changes at 2500 and 1400 cm^{-1}, which arise from the hydrogen-bond network and the carboxylate groups around the Mn_4CaO_5 cluster (Figure 4 and Table S1), suggest that the change in this phase is not a local event around $Y_Z^\bullet$ but involves the interaction change of the Mn_4CaO_5 cluster. It can thus be concluded from the TRIR data that water molecules change their positions around $Y_Z^\bullet$ and the Mn_4CaO_5 cluster in the ~100 μs phase.

This conclusion is consistent with a proposal in previous theoretical studies that W3, coordinated with Ca and indirectly interacting with $Y_Z^\bullet$ via another water molecule, moves to Mn4 or Mn1 in the S_2 state (Figure 6), coupling with the interconversion between the open and closed cubane conformations.[21,24,25,27] Such a water movement from the Ca^{2+} site to Mn4/Mn1 should induce changes in the hydrogen-bond network around $Y_Z^\bullet$ and the Mn_4CaO_5 cluster. Note that although the interconversion of the two conformations could be reflected in the change at 1400 cm^{-1}, similar infrared features in the COO^- region between them[43,49] hamper clear detection. The involvement of W3 in the water insertion process was also supported by a recent FTIR study by Debus and co-workers, where one of the bending vibrations of water molecules in the $S_2 \rightarrow S_3$ transition was significantly altered by replacement of Ca^{2+} with Sr^{2+}.[56] Internal proton transfer from a water ligand to a nearby water or amino acid residue could be coupled with this water insertion process; for example, a proton transfer from W1 to D1-Asp61 has been suggested in theoretical studies.[20,22,26] Water insertion into the Mn site is also consistent with the octahedral geometry of all four Mn ions in the S_3 state previously observed in an EPR study,[57] while the elongation of the Mn−Mn distance in this transition was detected by EXAFS.[58] The movement of W3 may induce further movements of water molecules to fill in the empty W3

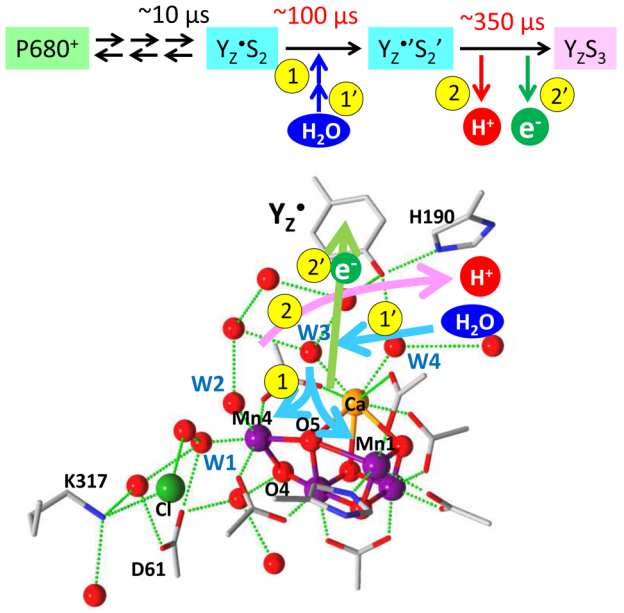

Figure 6. Mechanism of the $S_2 \rightarrow S_3$ transition suggested from the TRIR results taking into consideration the previous theoretical studies.[21,24,25,27] The ~100 μs phase is assigned to the transfer of a water molecule (possibly W3) from the site near $Y_Z^\bullet$ to a Mn ion (1), which induces the rearrangement of a hydrogen-bond network around $Y_Z^\bullet$ and insertion of a new water molecule to the vacant site (1′). The ~350 μs phase is attributed to electron transfer (2′) coupled with proton release (2), where the latter is a rate-limiting step. In our mechanistic model, a proton/water pathway via the Y_Z site is preferred to that via the D1-Asp61 site. Atomic coordinates from the X-ray crystallographic structure (PDB code: 4UB6)[8] were used to draw the WOC model.

site, as has been suggested by previous FTIR studies.[17−19] If the moved W3 functions as a substrate, this scheme of water insertion is consistent with the previous mass spectrometry studies, which concluded that both of two substrates are bound to the Mn_4CaO_5 cluster already in the S_2 state.[59,60] The observation of the change in the hydrogen-bond network around $Y_Z^\bullet$ and the above proposal of the movement of a water molecule near $Y_Z^\bullet$ also explain the blockage of the $S_2 \rightarrow S_3$ transition by Ca^{2+} depletion.[1,29] We recently showed that Ca^{2+} depletion or Ba^{2+} substitution diminished a broad band of the water network at 3200−2500 cm^{-1}, indicative of the destruction of a solid water network near Ca and Y_Z.[28] The change in the hydrogen-bond structure around $Y_Z^\bullet$ in ~100 μs may increase the $Y_Z^\bullet$ stability and hence shift the $P680^+ \leftrightarrow Y_Z^\bullet$ equilibrium to the $Y_Z^\bullet$ side.[4] This equilibrium shift was reflected in a relatively large contribution of the $P680^+$ decay at 4000 cm^{-1} to the ~100 μs phase (Figure 4 and Table S1).

The observation that the main phase of ~350 μs showed a KIE of 1.9, which is higher than 1.4−1.5 as a typical KIE of proton transfer in solution,[54,55] and no other high KIE phase was detected before this phase, strongly suggests that electron transfer in the $S_2 \rightarrow S_3$ transition is coupled to proton release (Figure 6). This KIE value highlights that the proton release reaction is a rate-limiting step in this phase. This proton release takes place most likely from a water ligand, or possibly from another water or an amino acid residue around the Mn_4CaO_5 cluster if internal proton transfer is coupled with the earlier ~100 μs phase of water transfer. A proton is released first to remove an excessive positive charge from the catalytic center to

DOI: 10.1021/jacs.6b11989
J. Am. Chem. Soc. 2017, 139, 2022−2029

decrease the redox potential, and then an electron is transferred from the Mn_4CaO_5 cluster to $Y_Z^{\bullet}$. We predict that, without an excessive positive charge, the rate of pure electron transfer should be similar to that of the $S_1 \rightarrow S_2$ transition, i.e., less than 100 μs. It is therefore reasonable that the relatively slow electron-transfer rate of ~350 μs in the $S_2 \rightarrow S_3$ transition is actually determined by the proton-transfer rate. Coupling of the proton transfer with electron transfer in the ~350 μs phase is also consistent with the previous observation of a large activation energy of this phase in the $S_2 \rightarrow S_3$ transition.[4,32] It is noteworthy that the similar KIE of ~2 has been observed in the lag phase of the $S_3 \rightarrow S_0$ transition at pH 5.5–6.5,[33,61] which most probably involves a proton release process.[3,13−16,31,36] The KIE values higher than the KIE of proton mobility in solution (1.4–1.5)[54,55] suggest that the proton-transfer pathways are formed by hydrogen-bonded chains involving amino acid residues in addition to water molecules.[55]

Three major pathways of proton release and water access have been suggested around the Mn_4CaO_5 cluster:[7,8,62−69] the pathway via the site near Y_Z, that via the Cl^- site, and the water channel starting from a water molecule interacting with O4. The latter two pathways involve D1-Asp61 at the entrance. We propose that the Y_Z pathway is used for the proton and water transfer in the $S_2 \rightarrow S_3$ transition (Figure 6), because the previous experimental data showed that site-directed mutations at D1-Asp61 and D2-Lys317 (a ligand to Cl^-) had little effect on the $S_2 \rightarrow S_3$ transition.[70−73] In particular, our observation of the rearrangement of the hydrogen-bond network around $Y_Z^{\bullet}$ in ~100 μs (Figure 2C) strongly supports the idea that water insertion takes place from the site near Y_Z. Nevertheless, recent theoretical works predicted the water insertion from the site near D1-Asp61 to Mn4.[23,26] If this were the case, it could be possible that the change in the hydrogen-bond network around Mn4 by water insertion is transferred to the $Y_Z^{\bullet}$ site via a water network between Mn4 and Y_Z (Figure 6), resulting in the change in the hydrogen-bond interaction at the $Y_Z^{\bullet}$ CO.

A remaining question is the consistency of the data in this study with the ~30 μs phase with a large KIE of 4–5 that was recently observed by Dau and co-workers.[13,14,37] They proposed that this phase arose from proton release from the cluster of water molecules located between $Y_Z^{\bullet}$ and Mn4.[13] However, we suggest that the proton release site responsible for the ~30 μs phase should not be involved in this water cluster, because there was no such phase in the changes in the $Y_Z^{\bullet}$ interaction (1514 cm^{-1}), the hydrogen-bond network between D1-Asp61 and Ca (2500 cm^{-1}), and the carboxylate groups around the Mn_4CaO_5 cluster (1400 cm^{-1}). It could therefore be possible that a proton is released from a water molecule or an amino acid side chain located a little away from the Mn_4CaO_5 cluster. If this were the case, the relatively large KIE (1.9) of the ~350 μs phase could be attributed to proton transfer from a water ligand of the Mn ion to the site of the first proton release that takes place in ~30 μs.

CONCLUSION

We investigated the reaction processes of electron, proton, and water transfers during the $S_2 \rightarrow S_3$ transition of photosynthetic water oxidation using TRIR spectroscopy. The ~100 μs phase was clearly observed as a significant change in the CO interaction of $Y_Z^{\bullet}$ and a lag phase before the Y_Z recovery (Figures 2C and 5). The KIE of this phase was relatively small (1.2), which makes the assignment of this phase to proton release less likely. This phase was attributed to the rearrangement of the hydrogen-bond network around $Y_Z^{\bullet}$. One likely scenario is the movement of a water molecule from the site near $Y_Z^{\bullet}$, possibly W3 ligated to Ca^{2+}, to a Mn ion, which has been suggested by previous theoretical studies.[21,24,25,27] Thus, the TRIR observation of the ~100 μs phase reinforces the crucial role of the hydrogen-bond network formed by water molecules near Y_Z and Ca in the $S_2 \rightarrow S_3$ transition.[28,74] In contrast, the subsequent ~350-μs phase, which showed a relatively large KIE of 1.9 (Table 1), was assigned to the electron transfer from the Mn_4CaO_5 cluster to $Y_Z^{\bullet}$ coupled with proton transfer, where the proton transfer functions as a rate-limiting step. We propose that this proton transfer corresponds to proton release from a water ligand, which should take place prior to the electron transfer to remove an excessive positive charge accumulated in the catalytic center in the S_2 state. Thus, the present TRIR study provides strong experimental evidence that in the $S_2 \rightarrow S_3$ transition, the rearrangement of the hydrogen-bond network around $Y_Z^{\bullet}$, possibly due to water movement, takes place before the electron transfer, which is coupled with a rate-limiting proton release. These results demonstrate that monitoring the reaction process using TRIR is an important method to clarify the whole mechanism of photosynthetic water oxidation.

ASSOCIATED CONTENT

Supporting Information

The Supporting Information is available free of charge on the ACS Publications website at DOI: 10.1021/jacs.6b11989.

Additional experimental details and characterization results(PDF)

AUTHOR INFORMATION

Corresponding Author

*tnoguchi@bio.phys.nagoya-u.ac.jp

ORCID

Takumi Noguchi: 0000-0002-3281-6827

Notes

The authors declare no competing financial interest.

ACKNOWLEDGMENTS

We thank Dr. Chihiro Kato for the technical assistance of time-resolved infrared measurement. This study was supported for Scientific Research from JSPS (24000018 and 24107003).

REFERENCES

(1) Debus, R. J. *Biochim. Biophys. Acta, Bioenerg.* **1992**, *1102*, 269–352.
(2) McEvoy, J. P.; Brudvig, G. W. *Chem. Rev.* **2006**, *106*, 4455–4483.
(3) Dau, H.; Haumann, M. *Coord. Chem. Rev.* **2008**, *252*, 273–295.
(4) Renger, G. *Biochim. Biophys. Acta, Bioenerg.* **2012**, *1817*, 1164–1176.
(5) Cox, N.; Messinger, J. *Biochim. Biophys. Acta, Bioenerg.* **2013**, *1827*, 1020–1030.
(6) Yano, J.; Yachandra, V. *Chem. Rev.* **2014**, *114*, 4175–4205.
(7) Umena, Y.; Kawakami, K.; Shen, J.-R.; Kamiya, N. *Nature* **2011**, *473*, 55–60.
(8) Suga, M.; Akita, F.; Hirata, K.; Ueno, G.; Murakami, H.; Nakajima, Y.; Shimizu, T.; Yamashita, K.; Yamamoto, M.; Ago, H.; Shen, J.-R. *Nature* **2015**, *517*, 99–103.
(9) Joliot, P.; Barbieri, G.; Chabaud, R. *Photochem. Photobiol.* **1969**, *10*, 309–329.
(10) Kok, B.; Forbush, B.; McGloin, M. *Photochem. Photobiol.* **1970**, *11*, 457–475.

DOI: 10.1021/jacs.6b11989
J. Am. Chem. Soc. 2017, 139, 2022–2029

(11) Schlodder, E.; Witt, H. T. *J. Biol. Chem.* **1999**, *274*, 30387−30392.
(12) Suzuki, H.; Sugiura, M.; Noguchi, T. *J. Am. Chem. Soc.* **2009**, *131*, 7849−7857.
(13) Klauss, A.; Haumann, M.; Dau, H. *Proc. Natl. Acad. Sci. U. S. A.* **2012**, *109*, 16035−16040.
(14) Klauss, A.; Haumann, M.; Dau, H. *J. Phys. Chem. B* **2015**, *119*, 2677−2689.
(15) Noguchi, T.; Suzuki, H.; Tsuno, M.; Sugiura, M.; Kato, C. *Biochemistry* **2012**, *51*, 3205−3214.
(16) Noguchi, T. *Biochim. Biophys. Acta, Bioenerg.* **2015**, *1847*, 35−45.
(17) Noguchi, T.; Sugiura, M. *Biochemistry* **2002**, *41*, 2322−2330.
(18) Suzuki, H.; Sugiura, M.; Noguchi, T. *Biochemistry* **2008**, *47*, 11024−11030.
(19) Noguchi, T. *Philos. Trans. R. Soc., B* **2008**, *363*, 1189−1195.
(20) Siegbahn, P. E. M. *Phys. Chem. Chem. Phys.* **2012**, *14*, 4849−4856.
(21) Bovi, D.; Narzi, D.; Guidoni, L. *Angew. Chem., Int. Ed.* **2013**, *52*, 11744−11749.
(22) Narzi, D.; Bovi, D.; Guidoni, L. *Proc. Natl. Acad. Sci. U. S. A.* **2014**, *111*, 8723−8728.
(23) Capone, M.; Narzi, D.; Bovi, D.; Guidoni, L. *J. Phys. Chem. Lett.* **2016**, *7*, 592−596.
(24) Shoji, M.; Isobe, H.; Yamaguchi, K. *Chem. Phys. Lett.* **2015**, *636*, 172−179.
(25) Isobe, H.; Shoji, M.; Shen, J. R.; Yamaguchi, K. *J. Phys. Chem. B* **2015**, *119*, 13922−13933.
(26) Retegan, M.; Krewald, V.; Mamedov, F.; Neese, F.; Lubitz, W.; Cox, N.; Pantazis, D. A. *Chem. Sci.* **2016**, *7*, 72−84.
(27) Ugur, I.; Rutherford, A. W.; Kaila, V. R. I. *Biochim. Biophys. Acta, Bioenerg.* **2016**, *1857*, 740−748.
(28) Nakamura, S.; Ota, K.; Shibuya, Y.; Noguchi, T. *Biochemistry* **2016**, *55*, 597−607.
(29) Yocum, C. F. *Biochim. Biophys. Acta, Bioenerg.* **1991**, *1059*, 1−15.
(30) Dekker, J. P.; Plijter, J. J.; Ouwehand, L.; van Gorkom, H. J. *Biochim. Biophys. Acta, Bioenerg.* **1984**, *767*, 176−179.
(31) Rappaport, F.; Blanchard-Desce, M.; Lavergne, J. *Biochim. Biophys. Acta, Bioenerg.* **1994**, *1184*, 178−192.
(32) Karge, M.; Irrgang, K. D.; Renger, G. *Biochemistry* **1997**, *36*, 8904−8913.
(33) Gerencsér, L.; Dau, H. *Biochemistry* **2010**, *49*, 10098−10106.
(34) Lydakis-Simantiris, N.; Ghanotakis, D. F.; Babcock, G. T. *Biochim. Biophys. Acta, Bioenerg.* **1997**, *1322*, 129−140.
(35) Razeghifard, M. R.; Pace, R. J. *Biochim. Biophys. Acta, Bioenerg.* **1997**, *1322*, 141−150.
(36) Haumann, M.; Liebisch, P.; Müller, C.; Barra, M.; Grabolle, M.; Dau, H. *Science* **2005**, *310*, 1019−1021.
(37) Zaharieva, I.; Dau, H.; Haumann, M. *Biochemistry* **2016**, *55*, 6996−7004.
(38) Christen, G.; Renger, G. *Biochemistry* **1999**, *38*, 2068−2077.
(39) de Wijn, R.; Schrama, T.; van Gorkom, H. J. *Biochemistry* **2001**, *40*, 5821−5834.
(40) Schilstra, M. J.; Rappaport, F.; Nugent, J. H. A.; Barnett, C. J.; Klug, D. R. *Biochemistry* **1998**, *37*, 3974−3981.
(41) Noguchi, T.; Ono, T.; Inoue, Y. *Biochim. Biophys. Acta, Bioenerg.* **1995**, *1228*, 189−200.
(42) Noguchi, T.; Sugiura, M. *Biochemistry* **2003**, *42*, 6035−6042.
(43) Nakamura, S.; Noguchi, T. *Proc. Natl. Acad. Sci. U. S. A.* **2016**, *113*, 12727−12732.
(44) Noguchi, T.; Sugiura, M. *Biochemistry* **2002**, *41*, 15706−15712.
(45) Iwai, M.; Suzuki, T.; Kamiyama, A.; Sakurai, I.; Dohmae, N.; Inoue, Y.; Ikeuchi, M. *Plant Cell Physiol.* **2010**, *51*, 554−560.
(46) Nakamura, S.; Nagao, R.; Takahashi, R.; Noguchi, T. *Biochemistry* **2014**, *53*, 3131−3144.
(47) Okubo, T.; Tomo, T.; Sugiura, M.; Noguchi, T. *Biochemistry* **2007**, *46*, 4390−4397.
(48) Debus, R. J. *Biochim. Biophys. Acta, Bioenerg.* **2015**, *1847*, 19−34.
(49) Onoda, K.; Mino, H.; Inoue, Y.; Noguchi, T. *Photosynth. Res.* **2000**, *63*, 47−57.
(50) Berthomieu, C.; Hienerwadel, R.; Boussac, A.; Breton, J.; Diner, B. A. *Biochemistry* **1998**, *37*, 10547−10554.
(51) Berthomieu, C.; Hienerwadel, R. *Biochim. Biophys. Acta, Bioenerg.* **2005**, *1707*, 51−66.
(52) Noguchi, T.; Sugiura, M. *Biochemistry* **2001**, *40*, 1497−1502.
(53) Suzuki, H.; Sugiura, M.; Noguchi, T. *Biochemistry* **2012**, *51*, 6776−6785.
(54) Agmon, N. *Chem. Phys. Lett.* **1995**, *244*, 456−462.
(55) Decoursey, T. E. *Physiol. Rev.* **2003**, *83*, 475−579.
(56) Kim, C. J.; Bao, H.; Burnap, R. L.; Debus, R. J. *Abstract of The 17th International Congress on Photosynthesis Research, Maastricht, The Netherlands*, August 7−12, 2016; p 28.
(57) Cox, N.; Retegan, M.; Neese, F.; Pantazis, D. A.; Boussac, A.; Lubitz, W. *Science* **2014**, *345*, 804−808.
(58) Yano, J.; Yachandra, V. *Chem. Rev.* **2014**, *114*, 4175−4205.
(59) Hillier, W.; Wydrzynski, T. *Phys. Chem. Chem. Phys.* **2004**, *6*, 4882−4889.
(60) Nilsson, H.; Krupnik, T.; Kargul, J.; Messinger, J. *Biochim. Biophys. Acta, Bioenerg.* **2014**, *1837*, 1257−1262.
(61) Bao, H.; Burnap, R. L. *Proc. Natl. Acad. Sci. U. S. A.* **2015**, *112*, E6139−E6147.
(62) Murray, J. W.; Barber, J. *J. Struct. Biol.* **2007**, *159*, 228−237.
(63) Ho, F. M.; Styring, S. *Biochim. Biophys. Acta, Bioenerg.* **2008**, *1777*, 140−153.
(64) Vassiliev, S.; Comte, P.; Mahboob, A.; Bruce, D. *Biochemistry* **2010**, *49*, 1873−1881.
(65) Bondar, A. N.; Dau, H. *Biochim. Biophys. Acta, Bioenerg.* **2012**, *1817*, 1177−1190.
(66) Ogata, K.; Yuki, T.; Hatakeyama, M.; Uchida, W.; Nakamura, S. *J. Am. Chem. Soc.* **2013**, *135*, 15670−15673.
(67) Bao, H.; Dilbeck, P. L.; Burnap, R. L. *Photosynth. Res.* **2013**, *116*, 215−229.
(68) Vogt, L.; Vinyard, D. J.; Khan, S.; Brudvig, G. W. *Curr. Opin. Chem. Biol.* **2015**, *25*, 152−158.
(69) Saito, K.; Rutherford, A. W.; Ishikita, H. *Nat. Commun.* **2015**, *6*, 8488.
(70) Dilbeck, P. L.; Hwang, H. J.; Zaharieva, I.; Gerencser, L.; Dau, H.; Burnap, R. L. *Biochemistry* **2012**, *51*, 1079−1091.
(71) Debus, R. J. *Biochemistry* **2014**, *53*, 2941−2955.
(72) Suzuki, H.; Yu, J.; Kobayashi, T.; Nakanishi, H.; Nixon, P.; Noguchi, T. *Biochemistry* **2013**, *52*, 4748−4757.
(73) Pokhrel, R.; Service, R. J.; Debus, R. J.; Brudvig, G. W. *Biochemistry* **2013**, *52*, 4758−4773.
(74) Lohmiller, T.; Shelby, M. L.; Long, X.; Yachandra, V. K.; Yano, J. *J. Phys. Chem. B* **2015**, *119*, 13742−13754.

DOI: 10.1021/jacs.6b11989
J. Am. Chem. Soc. 2017, 139, 2022−2029